

Space magnetometer based on an anisotropic magnetoresistive hybrid sensor

P. Brown, B. J. Whiteside, T. J. Beek, P. Fox, T. S. Horbury, T. M. Oddy, M. O. Archer, J. P. Eastwood, D. Sanz-Hernández, J. G. Sample, E. Cupido, H. O'Brien, and C. M. Carr

Citation: [Review of Scientific Instruments](#) **85**, 125117 (2014); doi: 10.1063/1.4904702

View online: <http://dx.doi.org/10.1063/1.4904702>

View Table of Contents: <http://scitation.aip.org/content/aip/journal/rsi/85/12?ver=pdfcov>

Published by the [AIP Publishing](#)

Articles you may be interested in

[Invited Article: Advanced drag-free concepts for future space-based interferometers: acceleration noise performance](#)

Rev. Sci. Instrum. **85**, 011301 (2014); 10.1063/1.4862199

[Highly sensitive anisotropic magnetoresistance magnetometer for Eddy-current nondestructive evaluation](#)

Rev. Sci. Instrum. **80**, 036102 (2009); 10.1063/1.3098946

[An optimized low-frequency three-axis search coil magnetometer for space research](#)

Rev. Sci. Instrum. **76**, 044502 (2005); 10.1063/1.1884026

[Space-based magnetometers](#)

Rev. Sci. Instrum. **73**, 3717 (2002); 10.1063/1.1510570

[Research and development of laser diode based instruments for applications in space](#)

AIP Conf. Proc. **458**, 604 (1999); 10.1063/1.57626

ZABER



Automate your research applications with Zaber's line of high precision positioning devices.

Low cost. Built-in controllers.
Simple to set up and easy to use.

Learn more at zaber.com ►

Space magnetometer based on an anisotropic magnetoresistive hybrid sensor

P. Brown,^{1,a)} B. J. Whiteside,¹ T. J. Beek,¹ P. Fox,¹ T. S. Horbury,¹ T. M. Oddy,¹ M. O. Archer,¹ J. P. Eastwood,¹ D. Sanz-Hernández,² J. G. Sample,³ E. Cupido,¹ H. O'Brien,¹ and C. M. Carr¹

¹Blackett Laboratory, Imperial College London, London SW7 2BW, United Kingdom

²EMM-NANO Consortium, K.U. Leuven, 3000 Leuven, Belgium

³Space Sciences Laboratory, University of California, Berkeley, California 94720, USA

(Received 13 June 2014; accepted 7 December 2014; published online 24 December 2014)

We report on the design and development of a low resource, dual sensor vector magnetometer for space science applications on very small spacecraft. It is based on a hybrid device combining an orthogonal triad of commercial anisotropic magnetoresistive (AMR) sensors with a totem pole H-Bridge drive on a ceramic substrate. The drive enables AMR operation in the more sensitive flipped mode and this is achieved without the need for current spike transmission down a sensor harness. The magnetometer has sensitivity of better than 3 nT in a 0–10 Hz band and a total mass of 104 g. Three instruments have been launched as part of the TRIO-CINEMA space weather mission, inter-calibration against the International Geomagnetic Reference Field model makes it possible to extract physical signals such as field-aligned current deflections of 20–60 nT within an approximately 45 000 nT ambient field. © 2014 AIP Publishing LLC. [<http://dx.doi.org/10.1063/1.4904702>]

I. INTRODUCTION

Magnetometers based on magnetoresistance (MR) have become increasingly popular in recent years^{1,2} due to the wide availability of sensor devices and low cost commercial off the shelf (COTS) chips.^{3–5} Applications such as space are increasingly utilising magnetoresistive technology, due to the very low mass and volume of the sensors (COTS MR sensors typically have a mass less than 1 g). Typical space applications are in the areas of on-board attitude orbit control systems (AOCS) particularly on nano and picosats.^{6,7} Several magnetoresistive magnetometers have been launched into space in recent years in place of more sensitive but higher resource fluxgates.⁸

The space applications requiring the highest performance magnetometers are scientific measurements for plasma and planetary missions where sub-nT accuracy is often required,⁹ in comparison to AOCS magnetometers, where 0.1 μ T uncertainty is typically sufficient.¹⁰ The key performance requirements for DC space science magnetometers are high sensitivity, low noise, excellent linearity over a wide dynamic range (e.g., 100 pT to up to 50 000 nT) and low or well characterised temperature drift of the sensor offset and gain.^{11,12} These properties need to be achieved while minimising the instrument resources (mass, power, volume) and the increasingly easy availability (and low cost) of MR sensors means that efforts to develop higher sensitivity MR magnetometers capable of detecting low amplitude science signals and competing with heritage fluxgates designs on vehicles such as planetary landers and nanosats has become increasingly popular.^{13,14}

Typically, older technology Anisotropic Magnetoresistive (AMR) permalloy sensors have been the preferred sensing option for DC MR magnetometers. This is for a

number of reasons: (i) they possess the highest detectivity at low frequencies (0–10 Hz) in comparison with other MR devices such as Giant or Tunneling magnetoresistance;¹⁵ (ii) they produce a bipolar output permitting measurement of positive and negative fields with a single device;¹⁶ (iii) as the sensor is anisotropic it is possible to modulate the direction of the easy axis and this provides a mechanism to track and compensate for the sensor bridge offset and maintain the sensor in its lowest noise operating state even in the presence of a large background ambient field.¹⁷ The modulation (commonly referred to as flipping) is achieved by driving bipolar current signals into on-chip coils that are aligned with the easy axis direction of the sensing element and integrated into the manufactured AMR package.¹⁸

In order to measure low-amplitude science signals aboard spacecraft (i.e., <100 nT), it is necessary to accommodate the magnetometer sensor on a deployable boom. This positions the sensor away from spacecraft magnetic fields produced by ferromagnetic material and current loops. To achieve the highest performance an AMR magnetometer will be configured as a null detector in a control loop featuring a constant flip drive at frequencies of a few hundred Hz. A vector magnetometer instrument is thus composed of a sensing triad of AMR sensors connected by harness to a spacecraft mounted electronics unit which houses the magnetometer drive, sense, and feedback functions.

Depending on the specific AMR sensor, flipping current amplitudes of up to 3 A for several microseconds can be required in order to achieve a full 180° rotation of the easy axis.¹⁸ In the case of picosats and nanosats, this presents a problem as the sensor boom harness must be made using high gauge wire in order to keep the mass as low as possible. Therefore, line losses in the harness will attenuate the flipping current and in the case of, for instance, a 1 m harness the

^{a)}patrick.brown@imperial.ac.uk

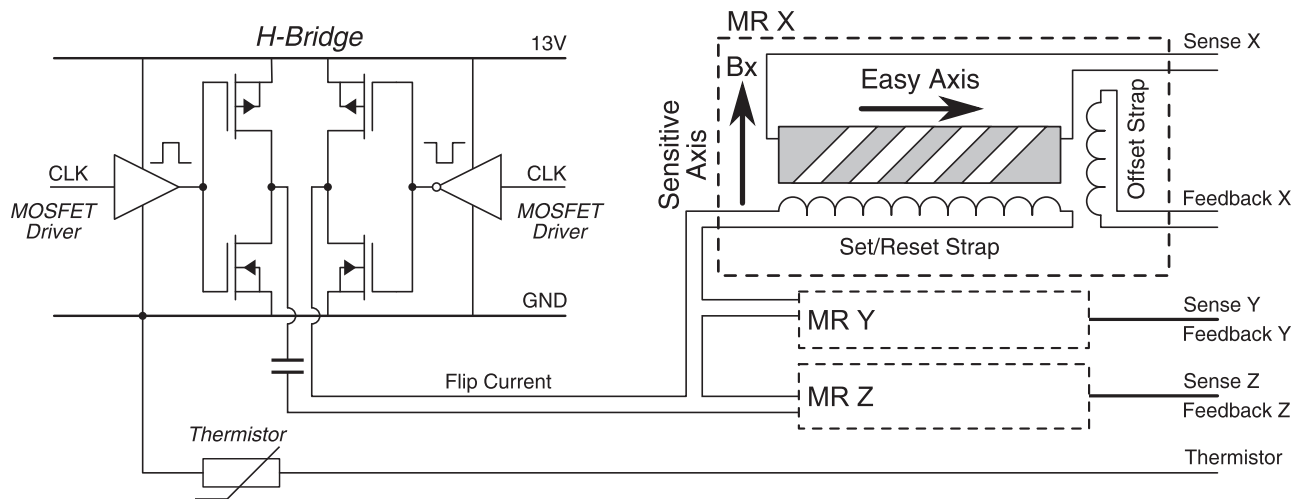


FIG. 1. A schematic of the electronics contained within the hybrid sensor. The sense, feedback, power, and CLK signals originate from the electronics card. The H-Bridge circuit is implemented as wire bonded die and the MRs are three discrete packages that form a vector triad.

attenuation is such that it effectively eliminates all the benefits (such as low noise and offset) of operating the sensor in a driven closed loop. A novel method of dealing with this problem is to migrate the flip current generation off the platform electronics and co-locate it with the AMR sensors. The current pulse is generated at the sensor, eliminating the need to overdrive a higher current pulse train from the platform down lossy cables. This technique saves power *and* permits the use of an arbitrarily long boom as it decouples the efficiency of the flipping drive from the harness length.

In this article, we present a compact dual-sensor vector magnetometer featuring an orthogonal AMR sensor triad combined with a hybrid flipping driver circuit. The magnetometer has been developed for a three CubeSat constellation mission called TRIO-CINEMA (CubeSat for Ions Electrons and Neutrals)^{19,20} where there was a specific requirement to accommodate a magnetometer sensor on an ultra-light 1 m stacer boom with a maximum harness mass of only 10 g. The combined sensor and driver is implemented on a ceramic tile and the only flipping related signals transmitted down the harness to the sensor are a voltage bias and drive clock. The sensor can thus operate in the optimum low noise state for connecting harness of any length.

II. MAGNETOMETER DESIGN

The magnetometer, called MAGIC (MAGnetometer from Imperial College), is composed of two functional blocks: the sensor head comprising the hybrid magnetic sensing element, implemented using three single axis Honeywell HMC1001¹⁸ AMR sensors, and an electronics card housing the magnetometer control electronics. Each single axis sensor is operated in a driven closed loop with first harmonic detection of the DC magnetic field²¹ and the feedback voltage sampled by an 8 channel 24 bit delta-sigma Analogue to Digital Converter (ADC). The hybrid sensor connects to the control electronics via a 1 m ultra-low mass harness (10 g without connector) comprised of 18 lines.

A. Hybrid AMR sensor

A schematic of the hybrid design is shown in Fig. 1. It is constructed on a single thick film low temperature co-fired ceramic (LTCC) tile and consists of three discrete single axis AMR sensors arranged in an orthogonal triad, N and P channel power metal oxide semiconductor field effect transistors (MOSFET) (FDN357N and FDT458P), inverting and non-inverting MOSFET drivers (TC4429 and MIC4420), and some discrete passives (thermistor and capacitors). The MOSFETs and the drivers are implemented as wire bonded die and covered in a glob top.

The HMC1001 was selected due to its superior noise floor at low frequency.¹⁵ It is comprised of a four element Wheatstone bridge with each half bridge Permalloy element having opposite magnetizations which doubles the sensor output. Each element is patterned with Barber pole shunts to shift the operating point to the most linear region of the AMR transfer function.²² The bridge bias, return, and the differential bridge output constitute four of the 8 pins on the device. The other four pins connect to a set-reset strap (parallel to the sensor easy axis) and offset strap (parallel to the sensor sensing (hard) axis), these are connected to the co-located drive pulse and remotely located feedback current generator, respectively.

The drive circuit is implemented on the hybrid in a totem pole H-Bridge configuration, formed from the dual P-N MOSFET and driver die. Bi-polar current pulses of 4 A are generated at 512 Hz and these are coupled into the 1.5 Ω set-reset straps (flip coils) of the three AMR sensors which are connected in series. The pulse train switches the easy axis orientation of the AMR elements in the bridge through 180° which causes the sensor output to change polarity resulting in a square wave output at the drive frequency. The capacitors (15 μ F tantalum and two 220 nF ceramics) were screened for magnetic signature (palladium-silver barrier were chosen in preference to nickel) and low electrical series resistance (ESR). The thermistor (Heraeus C220 Pt 100) was also verified non-magnetic by screening. As screening of the

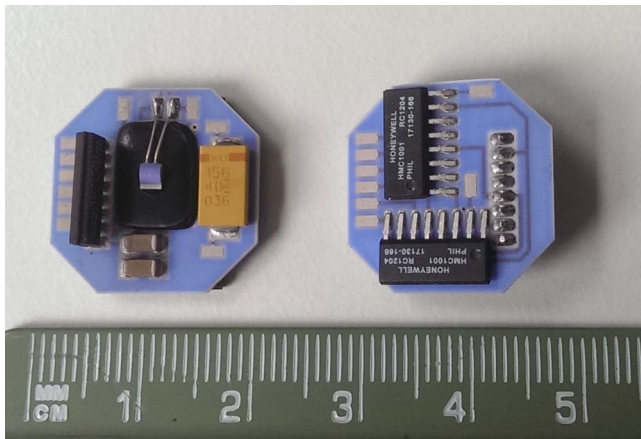


FIG. 2. Image of the hybrid chip from above and below. On the left hand side is the out of plane AMR sensor (Bz), the passives, and the black glob-top that covers the MOSFET die. The right hand side shows the in-plane AMR sensors (Bx,By).

MOSFETs and driver die was not possible the magnetic signature of the assembled hybrid device was also measured and found to be below the sensitivity threshold of the screening magnetometer (<0.1 nT).

The generation of the flipping current pulses locally on the hybrid means the only signals relating to the sensor drive function transmitted down the harness are a 13 V bias for the H-Bridge and the 512 Hz drive clock, which is generated on the main electronics card. This permits the use of extremely high gauge wire (36 AWG magnet wire was mandated for TRIO-CINEMA) while maintaining the ability to deliver short high current drive spikes into the set-reset straps.

The hybrid has dimensions of $2\text{ cm} \times 2\text{ cm} \times 0.5\text{ cm}$ and a mass of $<1\text{ g}$. All component parts used in the hybrid are commercial grade, however both the semiconductor die parts and capacitors are available as radiation hardened space

qualified versions. A photo displaying the two sides of the hybrid showing the orthogonal arrangement of the AMR chips is shown in Fig. 2. In the flight configuration, the hybrid is housed inside a $2\text{ cm} \times 2\text{ cm} \times 2\text{ cm}$ aluminium casing and held in a fixed position through the use of resin spacers. The whole head is potted in epoxy to provide both mechanical stability and to increase the thermal inertia to limit rapid temperature changes inside the MR sensors (e.g., as the sensor goes in and out of eclipse).

B. Control electronics

The electronics card houses the drive and sense analogue electronics and a 24 bit ADC (TI ADS1217). A schematic of the control electronics is shown in Fig. 3. Both analogue and digital electronics operate off a single ended 5 V supply and a 17 V line (which is dropped to 13 V) provides the bias for the H-Bridge flipping. There are six individual control loops in total, three for the three axis hybrid and three for a second orthogonal sensor triad of HMC1001s that are housed on the electronics card itself. The sensor triad housed on the electronics card is referred to as the Inboard (IB) sensor and the harness connected sensor is called the Outboard (OB) sensor. The inboard sensor was included for the purpose of redundancy in case of failure of the outboard hybrid sensor or harness connection. Each individual loop for the outboard sensor axes is composed of a differential low-noise pre-amp which amplifies the low amplitude flipped signal in parallel with an analogue offset compensator to remove the bridge offset as described previously.²¹ The DC centred signal is then demodulated and fed to an integrator which is used to control a feedback current via an op-amp, the output current of the op-amp flows down the harness to the offset strap which thereby closes the loop. The output of the integrator is directly proportional to the field component along the sensitive

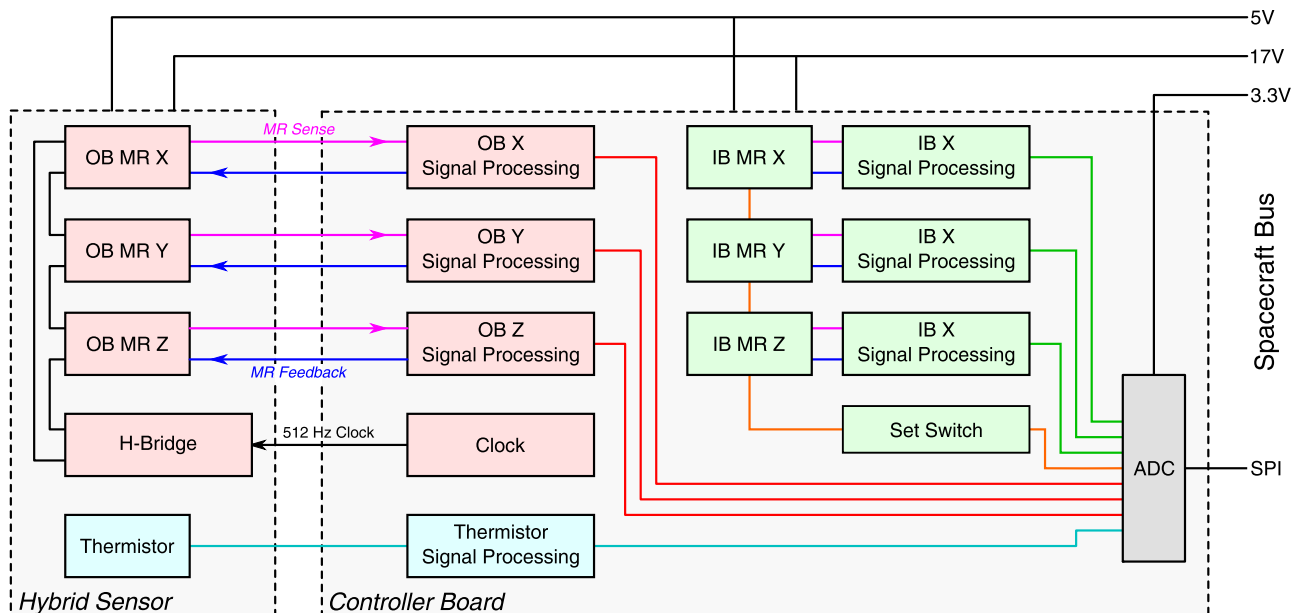


FIG. 3. Magnetometer block diagram. The hybrid sensor is connected to the controller board via a 1 m harness. The controller board contains the signal processing control for the hybrid, the complete inboard vector magnetometer, and ADC.

axis of the HMC1001 and this is fed into a channel of the ADC via a simple anti-aliasing filter (-3 dB 16 Hz). All op-amps are OP-484s from Analog Devices. The ADC includes a built-in 8 channel multiplexer and this is used to switch the input between the output filter of the 6 magnetometer channels (outboard and inboard). The other two channels are used to monitor the 5 V bus voltage (as it moves so does the 2.5 V ADC reference) and the hybrid sensor thermistor reading (which is also conditioned using an OP-484).

The ADS1217 is a second order delta-sigma modulator. The modulator sample rate is set by the Master Clock divided by 128. Off board communications are performed through the ADC using a Serial Peripheral Interface (SPI). Code was developed on a Teensy micro-controller (based on an Atmel ATmega32U4 microprocessor) and used to switch the ADC channel, sample the input, and apply an in-built digital filter which is configured over the SPI link. Several filters are available and a “sinc³” filter was chosen in a trade-off between settling time and bandwidth as it offers the lowest noise and highest effective number of bits (ENOB) at the expense of settling time, which in turn limits the vector sample rate. For the TRIO-CINEMA implementation multiple vector cadences were required:

- a low sensitivity, low power Attitude Mode (4 Hz) sampling the inboard sensor
- a high sensitivity, high power, Science Mode (8 Hz) sampling the outboard hybrid sensor
- a diagnostic, high power “Gradiometer Mode” (also 8 Hz) sampling the outboard hybrid sensor and inboard sensor at the same rate.

This use of different cadences meant the on-board digital filter has to be configured differently for each instrument mode.

The filter is configured through a programmable on-chip register storing the decimation setting, calculated according to

$$F_{Dec} = 0.95 \left(\frac{f_{osc} \times \Delta t}{128} \right), \quad (1)$$

where F_{Dec} corresponds to the filter decimation, f_{osc} is the ADC master clock frequency (222 Hz), and Δt is the time between component samples; the 128 is the delta-sigma ADC modulation factor and the 0.95 allows for 5% tolerance on the sampling to ensure the ADC settles before acquiring the next sample. The Δt corresponds to one quarter of the transmitted 8 Hz vector sample period in Science Mode (one quarter because each vector packet corresponds to the individual Bx, By, Bz, components sampled consecutively followed by a temperature reading with a 31.25 ms sample interval). Attitude mode sampling is configured differently; as it has a smaller 4 Hz cadence it was feared that for the crucial period where the CubeSat would use the Attitude Mode to autonomously de-tumble and spin up after release from the carrier spacecraft, the component samples of each attitude vector should have the minimal phase delay possible. Consequently, the phase delay between component samples is actually much smaller than a nominal one quarter of the 4 Hz vector rate (7.825 ms as opposed to 62.5 ms is used) with a much longer lag between successive vectors than in Science Mode where

the overall transmitted vector rate is higher but the phase lag between each individual components of each vector is larger and all samples are equally spaced in time.

In the case of Science Mode, the decimation is therefore 324 (for a Δt of 31.25 ms) and in Attitude Mode it is 80 (for a Δt of 7.8125 ms). The as-used value of F_{Dec} is taken as a multiple of 4 nearest to the calculated theoretical value as this optimises the data-ready time period within the ADC.²³

The higher sensitivity in science mode is achieved by virtue of the fact that the hybrid sensor is run with continuous flipping as well as being separated a meter from the electronics. By contrast the Attitude mode samples vectors from the sensors housed on the electronics card which are not continuously flipped although they do receive a single set pulse on mode entry.

The ADC also includes a number of general purpose IO lines, four of which are used, and these can be set via SPI command. These bits were used to configure hardware elements of the electronics card (such as switch on-off of the flipping drive) in accordance with a set of defined telecommands.

While the magnetometer was initially developed for low field applications such as planetary and lunar landers (target ambient field <5000 nT) as the first flight opportunity was to be the TRIO-CINEMA CubeSat launching to Low Earth Orbit (LEO), a large dynamic range was required. A range of $\pm 57\,500$ nT was implemented with 0 nT corresponding to 2.5 V input to the ADC channel, which corresponds to a nominal scale factor of 23 000 nT/V. This caused some problems for the feedback and overall loop stability which is discussed further in Sec. IV.

Table I details the basic instrument properties and parameters including the hardware configuration and decimation for the different instrument modes. The magnetometer is very low mass (total mass of the entire instrument is 104 g including 1 m harness) and power consumption varies within the range (0.14 W–0.5 W) according to the selected mode. Fig. 4 shows a photo of the entire instrument.

III. MAGNETOMETER CALIBRATION AND PERFORMANCE

Test and calibration of the magnetometer has been performed for the three TRIO-CINEMA flight units, concentrating on characterization of the outboard hybrid sensor operation in Science Mode. Noise, offset, and offset temperature drift have been measured in the laboratory using a three layer mu-metal shield tank with an integrated single axis solenoid stimulus coil and a highly accurate three axis reference flux-gate magnetometer.²⁴

The sensitivity of the magnetometer is shown in Fig. 5 for one axis under the application of a 0.05 Hz sine wave. We can see that the 10 nT amplitude sine wave is clearly resolved. A power spectral density amplitude of the magnetometer digital output in Science Mode for all three axes is plotted in Fig. 6. The detectivity of the three axes averaged around 1 Hz are as follows: Bx (324 pT Hz^{-1/2}), By (339 pT Hz^{-1/2}), and Bz (312 pT Hz^{-1/2}). The magnetometer noise density at 1 Hz is greater than that previously reported for our single

TABLE I. Instrument properties.

(a) Basic instrument properties			
Mass	33 g (potted sensor and 1 m harness) 71 g (electronics) 104 g (total)		
Volume	Sensor head 10 cm ³ Electronics 173 cm ³ (9×9.6×2 cm)		
Range	±57 500 nT		
Digital resolution	0.2 nT (19 bit transmission)		
−3 dB point	16 Hz		
Noise density	150 pT Hz ^{−1/2} (above 1 Hz)		
Operational temperature	−50 °C to +60 °C (electronics) −120 °C to +80 °C (sensor)		
(b) Mode specific properties. IB = Inboard, OB = Outboard			
Instrument mode	Attitude	Science	Gradiometer
Operational sensor	IB only	OB only	IB and OB
Flip frequency (Hz)	None	512	512 (OB)
Sensitivity (nT)	10	2	IB=10, OB=2
Cadence (vectors s ^{−1})	4	8	8 from both
ADC sample rate (Hz)	128	32	64
Decimation (F_{Dec})	80	324	160
Bus rails (V)	3.3, 5	17, 5, 3.3	17, 5, 3.3
Power (mW)	140	425	560

axis magnetometer design.²¹ A noise test was subsequently performed on one axis of the hybrid output at the input to the ADC and this is plotted in the inset of Fig. 6 together with that of the reference fluxgate. The noise density of the MR output at 1 Hz is 38 pT Hz^{−1/2} compared to 8 pT Hz^{−1/2} for the fluxgate. This suggests that the digitization of the analogue output is contributing significantly to the overall magnetometer noise level. This is an area to be targeted for improvement in future designs.

Longer term drift of the hybrid sensor is shown in Fig. 7 where the hybrid MR sensor is fitted within the mu-metal shield and operated in the laboratory over several days. We can see a slow periodic variation in the time series of all three axes, the drift is assumed to be offset drift with temperature.

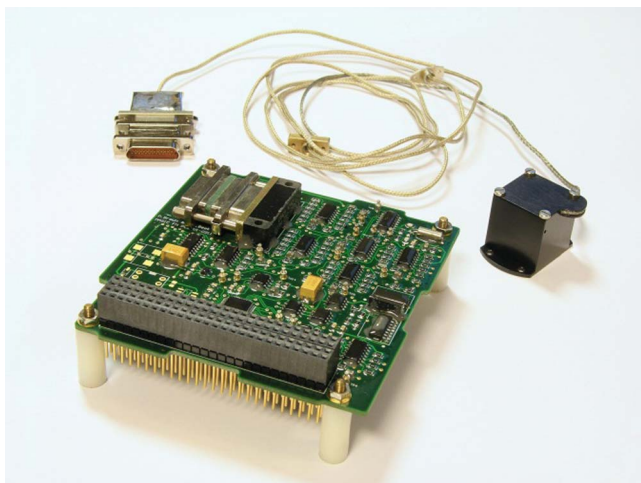


FIG. 4. Photo of one of the Trio-CINEMA flight instruments.

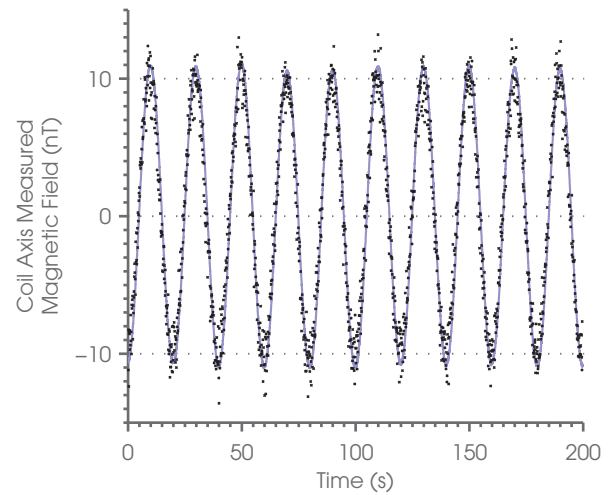


FIG. 5. A 0.05 Hz sinusoidal magnetic field applied along one axis of the hybrid with an amplitude of 10 nT. The hybrid output (dots) is compared to a reference fluxgate measurement (line).

Inter axis misalignments and gains have been determined using a rotation table at Imperial's non-magnetic calibration facility located in Staffordshire, UK. The sensor calibration matrix transforms the measured magnetic field vector from the non-orthogonal sensor frame into an orthogonalised reference frame in accordance with the following equation:

$$\mathbf{B}_c = \mathbf{C}_m(\mathbf{B}_m - \mathbf{O}), \quad (2)$$

where \mathbf{B}_m is the measured vector, \mathbf{O} is measured offset vector, \mathbf{C}_m is a 3×3 calibration matrix, and \mathbf{B}_c is the calibrated vector. The off diagonal elements of \mathbf{C}_m corresponding to the 6 inter-axis misalignment and diagonal elements correspond to the gain values of the individual sensor x, y, z axes. The calibration matrix has been determined as follows: the hybrid sensor and reference fluxgate are mounted onto Tufnel jigs that have a low mechanical tolerance. The sensor offset vector, \mathbf{O} , is measured using a shielding can fitted with a mounting track for the two jigs. After this the reference fluxgate is fixed to the centre of the rotation table and the average of Earth's magnetic field is measured through a 180° rotation. The reference is then replaced with the hybrid sensor and rotated through 6 different 90° rotations. The jig ensures an accurate 90° rotation when rotating the axis that is not in the plane of the rotation table. The hybrid data are then fitted by an iterative least squares algorithm to the fluxgate data under the assumption that the ambient field has been constant for the duration of the measurement of the two sensors. Once the matrix \mathbf{C}_m has been calculated a second set of 6 rotation measurements are taken with the hybrid and the calculated matrix is applied to the data to ensure that the calibrated field is within an acceptable error to that of the fluxgate. The calibration procedure is repeated if the residual error is greater than 1%.

Six magnetometers have been calibrated to date and the calibration results are shown in Table II. In each case, the sensor has been potted inside its aluminium housing so the mechanical orientations of the three individual HMC1001 sensors are rigidly fixed. As they are only visually aligned they do not form a perfect orthogonal triad and deviations of up

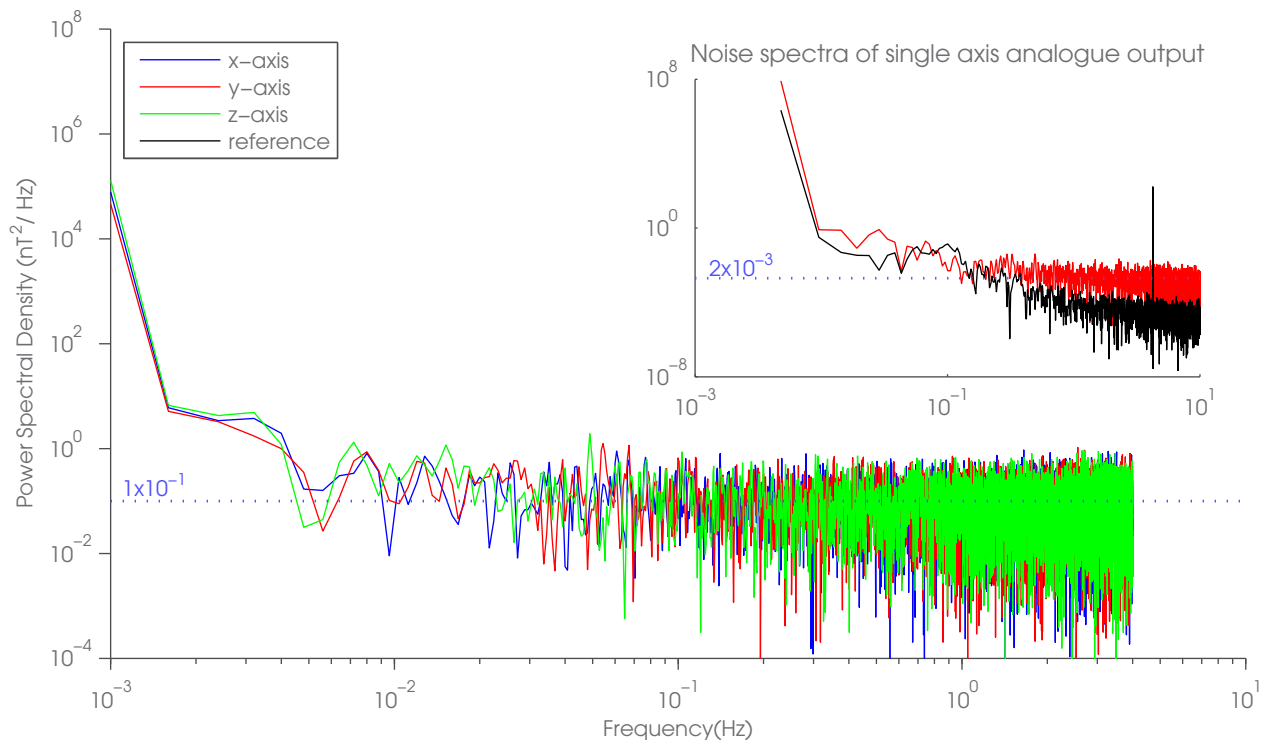


FIG. 6. Power spectral density of the three axes from the outboard sensor in Science Mode. The inlay is a power spectral density of the y-axis with the same setup but before digitisation together with a co-located with a reference fluxgate sensor, the noise of the y-axis is significantly reduced.

to a few degrees can occur, however, this is not a problem as long as the misalignments are known from the ground calibration. Existing methods of in-flight determination of calibration parameters use, for example, Fourier based techniques applied to spin stabilised spacecraft²⁵ and the International Geomagnetic Reference Field (IGRF) for LEO.²⁶ Such tech-

niques may be modified for application to TRIO-CINEMA in principle.

It can be seen from Table II that the offsets are in the range of a few hundred nT up to 2000 nT. This offset is comprised of electrical and sense effects. There are several different sources of electrical errors that contribute to the offset: these are caused by non-ideal op-amp behavior, small resistor mismatch, and input bias currents. The Wheatstone bridge offset and demodulation offset are almost negligible due to the active compensation provided by a feedback integrator at the preamplifier stage. The sense effects may be due to stray magnetic fields within the hybrid as a result of the flipping current. The sense offsets can be nulled using additional current injection into the offset strap but these are still susceptible to temperature effects. Options to improve the overall offset performance and stability are discussed in Sec. IV.

Fig. 8 plots the magnetometer output against the temperature of the sensor while within a dewar surrounded by a three layer magnetic shielding. The temperature was varied between -20°C and $+20^{\circ}\text{C}$. We can see that the Z axis has the worst drift of $38.4\text{ nT }^{\circ}\text{C}^{-1}$ and the Y axis has the smallest drift of $3.5\text{ nT }^{\circ}\text{C}^{-1}$. As the sensors are inside a low field environment we associate the observed drift with a changing sensor offset. The observed drift is not as good as that previously reported for the case of using standalone HMC1001 sensors driven from an electronics card²¹ but is comparable to the offset drift observed by Včelák,²⁷ further investigation is required to determine if there is an increased thermal susceptibility due to use of the hybrid sensor design.

Calibration residuals for two of the magnetometer models are plotted in Fig. 9. In both cases, the residual error to the

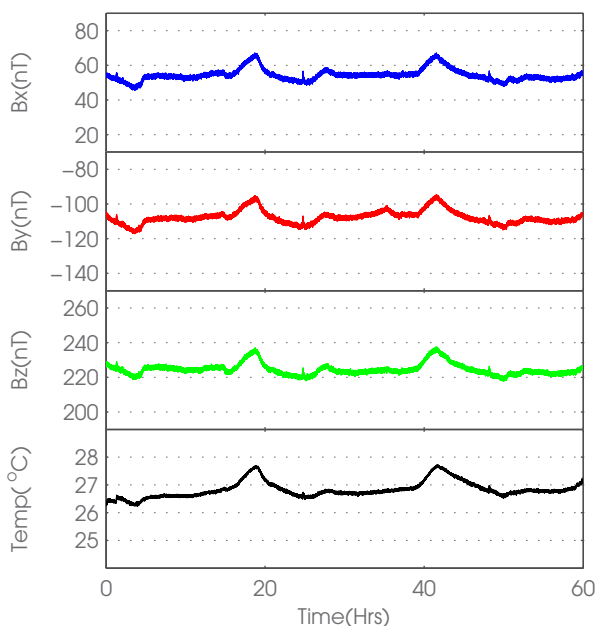


FIG. 7. Sensor output drift as a function of time with the temperature variation measured via the hybrid thermistor. The overall trend however is still clearly visible.

TABLE II. Hybrid sensor calibration results for several of the MAGIC instruments. Models FM2 and FM3 are currently in-flight, Models FM4 is a flight ready spare, EM is an engineering models. ND is not determined.

Cal. Parameter	Gains (nT V^{-1})			Offsets (nT)			Calibration matrix elements (C_{ij})								
	G_x	G_y	G_z	O_x	O_y	O_z	C_{11}	C_{12}	C_{13}	C_{21}	C_{22}	C_{23}	C_{31}	C_{32}	C_{33}
FM2	23 205.84	24 782.01	24 151.03	239	-705	-426	ND	ND	ND	ND	ND	ND	ND	ND	ND
FM3	22 634.78	22 908.70	23 179.38	-497	-102	-230	ND	ND	ND	ND	ND	ND	ND	ND	ND
FM4	20 757.11	20 256.54	20 300.88	912	255	1593	0.902	0.055	0.027	-0.009	0.881	0.008	0.027	0.015	0.883
FM5	22 155.90	21 781.69	21 310.42	130	584	-1514	0.963	0.013	-0.018	-0.011	0.947	-0.014	0.001	-0.013	0.927
EM3	21 089.62	22 032.57	24 242.12	232	70	811	0.962	-0.012	-0.024	0.053	0.958	0.011	0.011	-0.003	1.054
EM3-C	22 076.09	21 919.00	20 802.81	-239	527	-839	0.960	-0.027	0.057	0.008	0.953	-0.017	0.042	-0.019	0.904

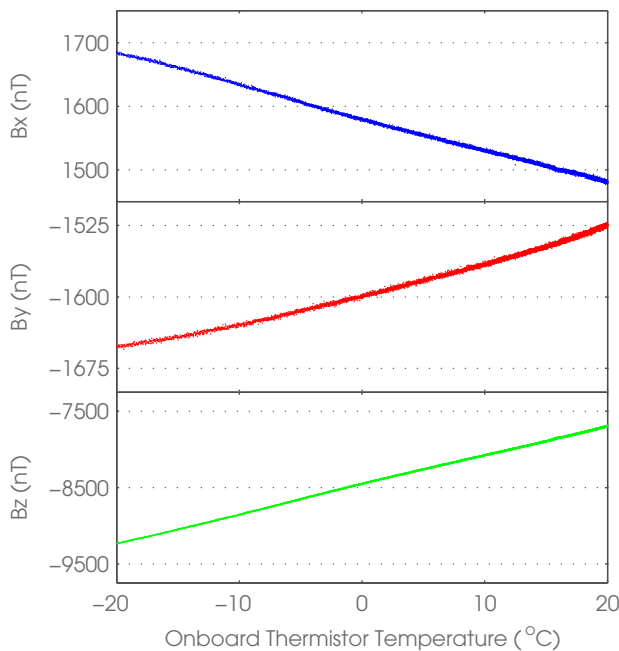


FIG. 8. Variation of sensor offset with temperature measured within a low magnetic field environment. The measured offset temperature dependence for X, Y, and Z is $-5.1 \text{ nT } ^\circ\text{C}^{-1}$, $3.5 \text{ nT } ^\circ\text{C}^{-1}$, and $38.4 \text{ nT } ^\circ\text{C}^{-1}$, respectively.

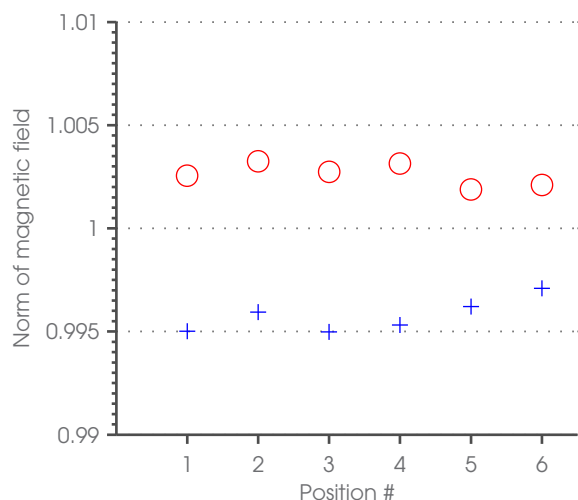


FIG. 9. The norm of the calibrated sensor output relative to the norm of the Earth's magnetic field, for the six positions used for calibration. A norm of 1 would imply the sensor output was identical to the actual field.

true vector is a magnitude better than 0.5% which is consistent with that achieved by Mohamadabadi who uses a similar method to calibrate a MR magnetometer.²⁸

One model of the magnetometer has also undergone formal qualification testing: mechanical vibration testing at $23.15 g_{rms}$ between 20 and 2000 Hz; and thermal vacuum (as part of one of the CINEMA CubeSats) in the range -20 to $+35$ $^\circ\text{C}$, with a 2 h soak time. The instrument remained fully functional after both tests. In addition, the hybrid sensor has undergone total ionising dose (TID) radiation testing up to 105 krad and maintained nominal functionality.²⁹

IV. DISCUSSION

While the magnetometer has very good sensitivity in the range 0-20 Hz the major performance limitation of the design at present is the offset and particularly the offset drift. The issue is partially mitigated if the ambient field of the target flight environment is substantially less than that in LEO, as would be the case in solar wind, where the maximum range required for, e.g., a magnetic field monitor at Lagrange point 1 is $\pm 500 \text{ nT}$.³⁰ In fact, the original pre-hybrid magnetometer design was targeted at much lower field ranges than Earth's field and this caused a problem when the operating range was scaled up to $\pm 57\,500 \text{ nT}$ for the TRIO-CINEMA hybrid design. It was found necessary to reduce the integrating feedback capacitance and add further gain at the integrator stage of each component channel in order to limit clipping and non-linearity while maintaining the needed bandwidth. This was a consequence of the relative large current (29 mA) required by the HMC1001 offset strap to null a $57\,500 \text{ nT}$ field and the inability of the op-amps used in the voltage to current converter to drive more than a 5 mA current. Therefore, the TRIO-CINEMA implementation effectively operates in a partial open loop configuration and therefore we expect it would exhibit worse offset drift than a fully closed loop implementation. However, we note that temperature drift of the sensor offset in space applications does not significantly degrade the science capability of the instrument as long as the temperature drift can be calibrated through analysis of the spinning sensor data and use of temperature dependent calibration matrix. This is possible on MAGIC due to recording of the hybrid temperature at the same cadence as the vector (8 Hz). Indeed, temperature dependent calibration in-flight is commonly

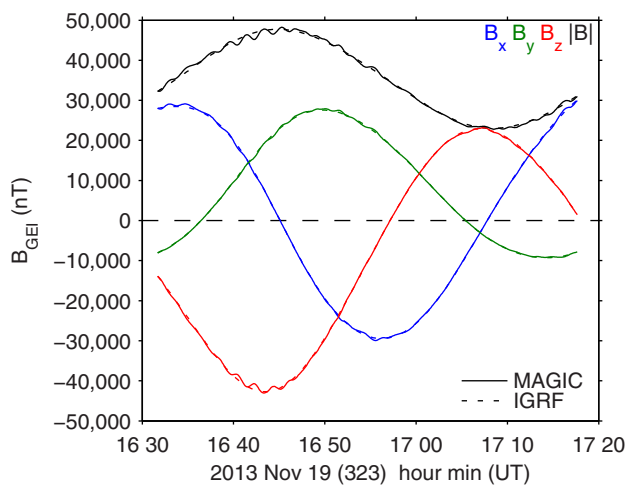


FIG. 10. Comparison of despun flight data from CINEMA 1 to IGRF. Oscillations due to residual uncertainties in de-spinning.

performed on fluxgate sensors on larger scientific spacecraft, especially in the case of smaller ring cores.³¹

Key areas of future work are to implement full current feedback drive in the Earth field range modes and improve the offset drift temperature. Improving the offset behavior will focus on more careful matching of the overall loop gain against the bandwidth and more complete elimination of the bridge offset in the offset compensator through use of an instrumentation amplifier or individual tuning of the compensator integrators. A further area to be studied is the effect of potential stray fields in the hybrid itself caused by circulating currents in the very high gauge induction wire. This is believed to be a non-negligible effect and may require a re-routing of the ceramic tile or change in wiring configuration.

Eventually it is planned to migrate the analogue control loop into the digital domain where the demodulation is performed inside a Field Programmable Gate Array (FPGA) or Application Specific Integrated Circuit (ASIC). This may offer the best option for real time tracking and compensation of the offset drift of the flipped sensor.

Three identical hybrid magnetometers have been launched, to date, on the three TRIO-CINEMA CubeSats into LEO. The first launch occurred on 13th September 2012 and the second two CubeSats were launched on 3rd November 2013. Unfortunately, in all three cases there was a problem with the spacecraft on-board antenna and so far there has been very limited data downloaded from the magnetometers. However, it has been established that at least one of the hybrid magnetometers (from the first launch) is fully functional one year on from launch and one of the second set is confirmed operational. Fig. 10 is a plot of the three field components from the hybrid sensor lasting approximately half an orbit (46 min). Though the spacecraft was tumbling, we have been able to determine the attitude of the sensor and calibrate the data by using the IGRF model.³² Temperature compensation of offsets and gains has also been integrated into the calibration model based on the measurements from the onboard thermistor. It can be seen that the magnetometer tracks the model well, with a root mean squared error of 1%. The difference between

the measured field and IGRF oscillate at periods of 4–10 min corresponding to the spin frequencies (rotation, nutation, and precession) of the spacecraft, due to drifting calibration parameters over this interval. The reason for the drift is likely due to the large and varying temperatures (~ 60 – 80 °C) experienced by CINEMA over this interval since the spacecraft had been in direct sunlight for ~ 3 days.

Nevertheless, the results are promising and demonstrate that the magnetometer design offers the prospect of ultra-low resource science **B** field measurements for future near-Earth, planetary, and deep space missions. Further subsequent analysis of this data interval has revealed the presence of Field Aligned Current (FAC) signatures in the range of 20–60 nT during quiet magnetospheric conditions, during passage across the auroral oval,³² which are consistent (but an order of magnitude smaller) than similar measurements made by Fish³³ who have recently published detection of FACs on the DICE CubeSat, also using an AMR magnetometer. These two results together verify that it is possible to resolve certain types of science signals in space using AMR based designs on small platforms.

ACKNOWLEDGMENTS

Financial support for the prototyping phase of the magnetometer has been provided by the UK Science Technology and Facilities Council (STFC Grant Code ST/K001051/1). Development of the hybrid sensor and flight units has been funded by ESA under the General Support Technology Programme (Contract No. 4000106430) and Permanent Open Call for Technology Demonstrators (Contract Code IC-1109-001). Dr. Martin Archer has been funded from STFC Grant Code ST/I505713/1. We particularly thank Dr. Alain Hilgers at ESA/ESTEC for his support. We also thank the teams of undergraduate students at SSL UCB and Imperial College who worked on the design and build of the TRIO-CINEMA CubeSats or support for MAGIC test and calibration. This article is dedicated to Professor Bob Lin, who was the inspiration and lead for the TRIO-CINEMA mission and who sadly passed away soon after the first CubeSat launch in September 2012.

¹J. Lenz and S. Edelstein, "Magnetic sensors and their applications," *IEEE Sens. J.* **6**, 631–649 (2006).

²M. J. Caruso, "Applications of magnetic sensors for low cost compass systems," in *Proceedings of the IEEE Position, Location and Navigation Symposium* (IEEE, 2000), pp. 177–184.

³A. Jander, C. Smith, and R. Schneider, "Magnetoresistive sensors for non-destructive evaluation," *Proc. SPIE* **5770**, 1–13 (2005).

⁴J. Vcelak, "Calibration of triaxial fluxgate gradiometer," *J. Appl. Phys.* **99**, 08D913 (2006).

⁵K. Mohamadabadi, C. Coillot, and M. Hillion, "New compensation method for cross-axis effect for three-axis AMR sensors," *IEEE Sens. J.* **13**, 1355–1362 (2013).

⁶H. Heidt, J. Puig-Suari, A. S. Moore, S. Nakasuka, and R. J. Twigg, "CubeSat: A new generation of picosatellite for education and industry low-cost space experimentation," in *Proceedings of the 14th Annual AIAA/USU Conference on Small Satellites*, SSC00-V-5, 2000.

⁷M. Michelena, I. Arruego, J. Oter, and H. Guerrero, "COTS-based wireless magnetic sensor for small satellites," *IEEE Trans. Aerosp. Electron. Syst.* **46**, 542–557 (2010).

⁸M. Michelena, "Small magnetic sensors for space applications," *Sensors (Basel, Switzerland)* **9**, 2271–2288 (2009).

- ⁹L.-Y. Liu, S.-B. Jiang, T.-L. Yeh, H.-C. Yeh, J.-Y. Liu, Y.-H. Hsu, and J.-Y. Peng, "The magneto-resistive magnetometer of BCU on the Tatiana-2 satellite," *Terres., Atmos. Oceanic Sci.* **23**, 317–326 (2012).
- ¹⁰A. Balogh, C. Carr, M. H. Acuna, M. W. Dunlop, T. Beek, P. Brown, K.-H. Fornacon, E. Georgescu, K.-H. Glassmeier, T. M. Oddy, and K. Schwingenschuh, "The cluster magnetic field investigation: Overview of in-flight performance and initial results," *Ann. Geophys.* **19**, 1207–1217 (2001).
- ¹¹G. M. Lerner and M. D. Shustert, "In-flight magnetometer calibration and attitude determination for near-Earth spacecraft," *J. Guid., Control, Dyn.* **4**, 518–522 (1981).
- ¹²M. H. Acuna, "Space-based magnetometers," *Rev. Sci. Instrum.* **73**, 3717–3736 (2002).
- ¹³A. Balogh, "Planetary magnetic field measurements: Missions and instrumentation," *Space Sci. Rev.* **152**, 23–97 (2010).
- ¹⁴W. Magnes and M. Díaz-michelena, "Future directions for magnetic sensors for space applications," *IEEE Trans. Magn.* **45**, 4493–4498 (2009).
- ¹⁵N. A. Stutzke, S. E. Russek, D. P. Pappas, and M. Tondra, "Low-frequency noise measurements on commercial magnetoresistive magnetic field sensors," *J. Appl. Phys.* **97**, 10Q107 (2005).
- ¹⁶M. J. Caruso, T. Bratland, C. H. Smith, and R. Schneider, "A new perspective on magnetic field sensing," *Sensors* **15**, 34–46 (1998).
- ¹⁷H. Hauser, P. Fulmek, P. Haumer, M. Vopalensky, and P. Ripka, "Flipping field and stability in anisotropic magnetoresistive sensors," *Sens. Actuators A* **106**, 121–125 (2003).
- ¹⁸Honeywell, "1- and 2-axis magnetic sensors HMC1001, 1002, 1021, 1022," Datasheet 900248, (2008).
- ¹⁹D.-H. Lee and R. P. Lin, "Kyung Hee University's WCU Project on Space Exploration in Lunar Orbit Research," *AAPPS Bull.* **19**, 18–23 (2009).
- ²⁰K. Vega, D. Auslander, and D. Pankow, "Design and modeling of an active attitude control system for CubeSat class satellites," in *Proceedings of the AIAA Modelling and Simulation Technologies Conference, August 2009* (AIAA, 2009), pp. 10–13.
- ²¹P. Brown, T. Beek, C. Carr, H. O'Brien, E. Cupido, T. Oddy, and T. S. Horbury, "Magnetoresistive magnetometer for space science applications," *Meas. Sci. Technol.* **23**, 059501 (2012).
- ²²M. Endoh, N. Shimizu, H. Yoda, and N. Waoatsuki, "Highly sensitive thin film magnetoresistive sensor with good linearity," in *Proceedings of the Fifth IEEE/CHMT International Design-to-Manufacturing Transfer Cycle Electronic Manufacturing Technology Symposium, 1988* (IEEE, 1988), pp. 210–214.
- ²³J. Wu, "Calibration routines and register value generation for the ADS1216, ADS1217 and ADS1218," Texas Instruments Application Note SBAA099 (Texas Instruments Inc., 2003), pp. 1–10.
- ²⁴C. Carr, P. Brown, T. L. Zhang, J. Gloag, T. Horbury, E. Lucek, W. Magnes, H. O'Brien, T. Oddy, U. Auster, P. Austin, O. Aydogar, A. Balogh, W. Baumjohann, T. Beek, H. Eichelberger, K.-H. Fornacon, E. Georgescu, K.-H. Glassmeier, M. Ludlam, R. Nakamura, and I. Richter, "The Double Star magnetic field investigation: Instrument design, performance and highlights of the first years observations," *Ann. Geophys.* **23**, 2713–2732 (2005).
- ²⁵E. L. Kepko, K. K. Khurana, M. G. Kivelson, R. C. Elphic, and C. T. Russell, "Accurate determination of magnetic field gradients from four point vector measurements - Part 1," *IEEE Trans. Magn.* **32**, 377–385 (1996).
- ²⁶J. C. Springmann and J. W. Cutler, "Attitude-independent magnetometer calibration with time-varying bias," *J. Guidance, Control, Dyn.* **35**, 1080–1088 (2012).
- ²⁷J. Včelák, P. Ripka, A. Platil, J. Kubík, and P. Kašpar, "Errors of AMR compass and methods of their compensation," *Sens. Actuators A* **129**, 53–57 (2006).
- ²⁸K. Mohamadabadi and M. Hillion, "An automated indoor scalar calibration method for three-axis vector magnetometers," *IEEE Sens. J.* **14**, 3076–3083 (2014).
- ²⁹B. J. Whiteside, P. Brown, T. J. Beek, T. S. Horbury, and C. M. Carr, "TID response of a hybrid AMR vector magnetometer," in *IEEE Radiation Effects Data Workshop record, Paris, 2014*, pp. 165–168.
- ³⁰J. Eastwood, P. Brown, T. Oddy, B. J. Whiteside, P. Fox, N. Adeli, T. J. Beek, C. M. Carr, and N. Barnes, "Magnetic field measurements from a solar sail platform with space weather applications," *Advances in Solar Sailing* (Springer Praxis Books, 2014), pp. 185–200.
- ³¹K.-H. Glassmeier, I. Richter, A. Diedrich, G. Musmann, U. Auster, U. Motschmann, A. Balogh, C. Carr, E. Cupido, A. Coates, M. Rother, K. Schwingenschuh, K. Szegö, and B. Tsurutani, "RPC-MAG: The fluxgate magnetometer in the ROSETTA plasma consortium," *Space Sci. Rev.* **128**, 649–670 (2007).
- ³²M. O. Archer, T. S. Horbury, P. Brown, J. P. Eastwood, T. M. Oddy, B. J. Whiteside, J. G. Sample, S. M. Imber, and T. K. Yeoman, "The MAGIC of CINEMA: First in-flight science results from a miniaturised anisotropic magnetoresistive magnetometer," *Space Sci. Rev.* (submitted).
- ³³C. S. Fish, C. M. Swenson, G. Crowley, A. Barjatya, T. Neilsen, J. Gunther, I. Azeem, M. Pilinski, R. Wilder, D. Allen, M. Anderson, B. Bingham, K. Bradford, S. Burr, R. Burt, B. Byers, J. Cook, K. Davis, C. Frazier, S. Grover, G. Hansen, S. Jensen, R. LeBaron, J. Martineau, J. Miller, J. Nelsen, W. Nelson, P. Patterson, E. Stromberg, J. Tran, S. Wassom, C. Weston, M. Whiteley, Q. Young, J. Petersen, S. Schaire, C. R. Davis, M. Bokaie, R. Fullmer, R. Baktur, J. Sojka, and M. Cousins, "Design, development, implementation, and on-orbit performance of the Dynamic Ionosphere CubeSat Experiment Mission," *Space Sci. Rev.* **181**, 61–120 (2014).